Full Length Article

Investigations of supported Au-Pd nanoparticles on synthesized CeO_2 with different morphologies and application in solvent-free benzyl alcohol oxidation

Xiaoliang Li[a], Jiangjiang Feng[a], Michal Perdjon[b], Rena Oh[c], Wei Zhao[a], Xiaoyang Huang[b], Shusen Liu[d],

[a] State Key Laboratory Breeding Base of Coal Science and Technology Co-founded by Shanxi Province and the Ministry of Science and Technology, Taiyuan University of Technology, Taiyuan 030024, Shanxi, PR China
[b] Cardiff Catalysis Institute, Centre for Doctoral Training in Catalysis, School of Chemistry, Cardiff University, Park Place, Cardiff CF10 3AT, United Kingdom
[c] Department of Chemistry, Seoul National University, Seoul 08826, South Korea
[d] Lignite Fly Ash Institute of Engineering & Technology, Xilingol Vocational College, Xilinhot 026000, Inner Mongolia, PR China

ARTICLE INFO

Keywords:
Benzyl alcohol oxidation
Au-Pd
CeO_2
Morphology
Solvent-free

ABSTRACT

Au-Pd bimetallic nanoparticles immobilized on series of CeO_2 supports with different morphologies, e.g., rod, cube, and polyhedrons were prepared through the deposition-precipitation method with a consequent in-vestigation on their catalytic performances for benzyl alcohol oxidation in the absence of solvent. The experi-mental results exhibited that the morphology of CeO_2 has a markedly impact on the catalytic performance of Au-Pd/CeO_2. In which Au-Pd supported on CeO_2 rod could achieve higher benzyl alcohol conversion than that supported on CeO_2 polyhedrons and CeO_2 cube, however, CeO_2 cube supported Au-Pd showed the highest selectivity towards the production of benzaldehyde. ICP-AES, XRD, Raman, N_2-BET, TEM, HAADF-STEM, and XPS were conducted to characterize the catalysts. The results revealed that the excellent behavior of Au-Pd/ CeO_2-rod in benzyl alcohol oxidation was closely related with the smaller size of CeO_2 particle, the higher concentration of oxygen defects in support and the higher number of Ce^{3+} and Pd^{2+} species on the catalyst surface. The present study on the morphologies of CeO_2 support in solvent-free benzyl alcohol oxidation would offer a notable approach for the future catalyst design.

1. Introduction

Gold-based catalysts were well reported to exhibit super catalytic activity in a lot of reactions, e.g. glycerol oxidation, WGS reaction, and selective hydrogenation of cinnamaldehydes, etc. [1–3]. Among the applied catalysts, Au-Pd bimetallic catalyst has shown its significant enhancement in catalysis, involving reactions of catalytic oxidation of benzyl alcohol, low-temperature methane oxidation and primary carbon-hydrogen bonds activation, direct formation of H_2O_2, etc. [4–7].

Direct synthesis of aldehydes with the corresponding primary al-cohols is a very important chemical industrial process as the aldehydes are the critical pharmaceutical intermediates. The traditional processes for the production of aldehydes involve the use of inorganic oxides (e.g. permanganate or chromate), which are not only high-priced but also environmentally-unfriendly [8]. Instead, producing aldehydes with O_2 or air as an environmentally-benign oxidant and noble metal as a catalyst has provided a novel approach to overcome the caused pollu-tion. Direct catalytic conversion of benzyl alcohol under solvent-free is one of the most studied examples. Bimetallic Au-Pd catalysts have at-tracted big research attention for benzyl alcohol oxidation reaction since the catalytic activity was enhanced by twenty-five-fold compare to Au catalyst alone whilst retaining the selectivity towards benzy-laldehyde, which was attributed to the electron transferring from Pd to Au [4]. As supports for Au-Pd nanoparticles, zeolite, titania, carbon, etc. have been widely used and reported, showing high catalytic perfor-mance under similar tested conditions [8–11].

There are many factors affecting the catalytic activity from the immobilized Au-Pd catalyst such as particle size, synthesis method, physico-chemical properties and morphologies of the support etc. As a typical catalyst support, CeO_2 has attracted significant research atten-tion owing to the excellent oxygen storage capacity, the closely inter-action between metal and support, and the capability of easy shuttling

Corresponding authors.
E-mail addresses: lixiaoliang@tyut.edu.cn (X. Li), liushusen@tsinghua.org.cn (S. Liu).

between Ce^{3+} and Ce^{4+} oxidation states. CeO_2 supported Au-Pd was reported to show outstanding catalytic performance in many reactions [11,12]. Interestingly, CeO_2 morphology could decide the exposure of reactive planes and further influence the particle size of active metal, the interaction between noble metal and CeO_2, and the dispersion of the precious metal. Recently, CeO_2 with different morphologies exposing different facets were prepared successfully and indeed exhibited dif-ferent catalytic activities in water-gas shift reaction [11,13]. Liu et al. synthesized CeO_2 rod under the protection of N_2 followed by in-situ load of Au and Pd nanoparticles applying surface redox mechanism between CeO_2 and noble metal to produce AuPd/CeO_2 rod catalyst, which showed high benzyl alcohol conversion and benzaldehyde selectivity [14]. David et al. also prepared Au-Pd/CeO_2 nanorod catalyst with sol-immobilization method using $NaBH_4$ as a reducing agent, which ex-hibited high catalytic activity in the same reaction under solvent-free condition [15]. In addition, Au-Pd supported on ceria-zirconia mixed oxide was also applied for the benzyl alcohol oxidation, a synergistic effect existed between Au and Pd during the reaction [16,17].

Up to now, only few reports focused on the influence of catalytic behavior of Au-Pd/CeO_2 caused by the morphology/crystal plane of CeO_2 in oxidation of benzyl alcohol. In the present research, CeO_2 with different morphologies (rod, cube, and polyhedrons) was synthesized by hydrothermal method and used as supports for immobilization of Au-Pd bimetal through deposition-precipitation approach with urea as precipitant. Systematic investigations were carried out on the impact of support morphology of Au-Pd/CeO_2 for benzyl alcohol oxidation under solvent-free.

2. Experimental

2.1. Chemical reagents and gases

The chemical reagents used in our experiments were all supplied by Aladdin company (Shanghai China) and used as received: benzyl al-cohol (99.8%, purity), Urea (99.5% metal basis), NaOH (99.9% metal basis), $Ce(NO_3)\cdot 6H_2O$ (99.95% metals basis), $PdCl_2$ (99.999% metals basis), and $HAuCl_4\cdot 3H_2O$ (≥99.9% trace metals basis). O_2 (99.999%, purity) was supplied from Taiyuan iron and steel corporation.

2.2. Synthesis of CeO_2

CeO_2 nanorods, nanopolyhedrons, and nanocubes were synthesized by employing hydrothermal method based on Mai et al.'s report [11]. For CeO_2 nanorods, 60 mL deionized water was applied to dissolve the 19.2 g sodium hydroxide and 20 mL deionized water was used to dis-solve the 1.736 g cerium nitrate hexahydrate, respectively. Subse-quently, the former was dripped into the latter. After stirring for 15 min, the mixed solution was injected into a 100 mL hydrothermal autoclave. Then the container was heated to 100 °C and hold for 24 h. When the obtained product was centrifuged and washed, the sample was dried at 105 °C for 12 h and calcined at 400 °C for 4 h to achieve the final product. For CeO_2 polyhedrons, we only changed the dosage of NaOH from 19.2 g to 0.32 g. For the preparation of CeO_2 with cubic shape, we only adjusted the hydrothermal temperature from 100 °C to 180 °C.

2.3. Au-Pd NPs immobilized on nanostructured CeO_2

Au-Pd nanoparticles immobilized on CeO_2 (rod, polyhedron, and cube) were prepared through the deposition-precipitation approach with urea as the precipitant. Typically, to fabricate the Au-Pd/CeO_2-rod, 2.00 mL aqueous solution of $HAuCl_4$ (5 mg Au/mL), 1.08 mL aqueous solution of $PdCl_2$ (5 mg Pd/mL), 0.985 g CeO_2-rod and 3.48 g urea were added into 100 mL H_2O, respectively. When the solution was stirred for 12 h at 80 °C. The autoclave was then cooled to ambient temperature, the obtained solution was aged for another 12 h. Subsequently, the precipitate was centrifuged, washed and dried. Finally, the obtained product was roasted at 300 °C for 2 h. For sim-plicity, CeO_2-rod, CeO_2-polyhedron, CeO_2-cube, Au-Pd/CeO_2-rod, Au-Pd/CeO_2 -polyhedron, and Au-Pd/CeO_2-cube catalysts were denoted as CR, CP, CC, ACR, ACP, and ACC, respectively.

2.4. Catalytic oxidation of benzyl alcohol

The evaluation experiment was performed in a mechanically stirred reactor (50 mL glass-lined, Anhui Kemi machinery Technology Co., Ltd, China). Typically, 15 mL benzyl alcohol and given mass of catalyst were introduced into the reactor, the reactor was sealed and purged for 5 times by O_2. Then, the autoclave was pressurized to 0.3 MPa with O_2 at ambient temperature. After the reaction vessel was heated to the preset temperature the stirring was set to1000 rpm to start the reaction, the oxygen reservoir was kept linking during the reaction for the purpose of replenishing the consumed oxygen. The mixture after reaction was analyzed by GC (FuLi GC9790, Zhejiang, China) equipped with FID and DM-5 column.

The benzyl alcohol conversion and the TOF values were calculated as follows:

$$X=\frac{(n_{benzylalcohol,in}-n_{benzylalcohol,out})}{n_{benzylalcohol,in}}\times 100\%;$$

$$TOF=\frac{n_{benzylalcohol,in}\times X}{(n_{Au}+n_{Pd})\times t};\ (X\ \ 15\%)$$

'n' is the molar mass; 't' is the reaction time;

2.5. Catalyst characterization

ICP-AES was performed to quantitatively analyze the Au-Pd con-tents of the prepared samples on an Agilent 735-ES instrument. Before measurements, the catalysts were dissolved in aqua regia for about 24 h. An ASAP2020 instrument was applied to analyze the BET surface area, pore diameter and pore volume of the prepared samples. The BET method and t-plot methods were used to get the specific area and mi-cropore volume. XRD was conducted on a powder diffractometer (Rigaku D/max-RC with CuKα), which was operated at 25 mA and 40 kV. The data was collected within 10–90° at a scanning speed of 8°/ min. Visible Raman spectra was carried out on a Raman microscope (Renishaw in Via) at ambient temperature. TEM was conducted on an electron microscope (JEM-2100) operated at 200 kV. HAADF-STEM was carried out on a FEI Titan Cubed Themis G2 300 aberration-cor-rected scanning transmission electron microscope manipulated at 300 kV. XPS was conducted on a PHI-1600ESCA spectrometer applying Mg-Kα at 1254 eV.

3. Results and discussion

For keeping the Au:Pd molar ratio at 1:1, the nominal loadings of Pd and Au on the ACR, ACP, and ACC were respectively 0.54 wt% and 1.00 wt% The actual concentration of Au and Pd determined by ICP-AES was summarized in Table 1, demonstrated that > 90% of Au and 83% of Pd were immobilized on the supports. The difference between

Table 1
Au and Pd bulk composition on the Au-Pd/CeO_2 catalysts.

Catalysts	Au (wt%)		Pd (wt%)		Au/Pd molar ratio
	Nominal	Actual	Nominal	Actual	
ACR	1.00	0.93	0.54	0.46	1.09
ACP	1.00	0.97	0.54	0.45	1.16
ACC	1.00	0.94	0.54	0.51	1.00

Note: The actual concentrations were determined by ICP-AES.

Table 2
Structural properties of the CeO_2 and Au-Pd/CeO_2 catalysts.

Samples	BET surface area m^2/g	Pore volume cm^3/g	Average pore diameter nm	CeO_2 crystalline size nm
CR	112	0.74	17.6	7.3
ACR	107	0.59	16.5	7.3
CP	82	0.32	5.2	10.2
ACP	79	0.28	5.0	10.2
CC	53	0.29	13.2	27.9
ACC	49	0.23	13.1	27.9

Note: CeO_2 crystallite size was calculated by Scherrer equation based on the XRD results.

nominal and actual concentration further verifies the existence of metal loss in the preparation process, which might be connected with the leaching of weakly adsorbed Au-Pd during filtration or washing process in the catalyst preparation.

The specific physical structural parameters of the CeO_2 supports and Au-Pd/CeO_2 catalysts were summarized in Table 2. For these three kinds of CeO_2, the BET surface area and the total pore volume are ar-ranged as follows: CR > CP > CC. However, CP presented the smallest pore diameter compared to the other two carriers. It is also found that these three physical parameters (surface area, average pore diameter, and pore volume) were inhibited to different extent after loading active components, which could be related to the pore blockage by immobilization of Au and Pd NPs.

XRD was conducted to analyze the structure of the prepared CeO_2 supports, ACR, ACP, and ACC, the corresponding patterns were dis-played in Fig. 1. Nine prominent peaks located at 2θ = 28.5, 33.1, 47.5, 56.3, 59.1, 69.4, 76.7, 79.2, and 88.4° were detected in CR, CP and CC. These peaks should be assigned to Miller indices (1 1 1), (2 0 0), (2 2 0), (3 1 1), (2 2 2), (4 0 0), (3 3 1), (4 2 0), and (4 2 2) crystalline planes of the typical Cerianite structure (PDF 34-0394). The average CeO_2 crys-tallite size of these samples were obtained by employing the Scherrer equation based on the diffraction peak information located at 28.5°, which demonstrated that the CeO_2 crystallite size in CC (27.9 nm) is significantly bigger than CP (10.2 nm) and CR (7.3 nm). And, there was no significant changes of XRD patterns happened after the support of Au-Pd NPs. It might be attributed to low concentration of metal and relatively smaller Au-Pd particle size compare to the supports (Au-Pd nanoparticles size ca 2–4 nm). The above results also demonstrated that the structure of CeO_2 supports, and the average particle size of CeO_2 were unaffected by the loading of Au and Pd nanoparticles.

It is generally accepted that Raman spectroscopy is another mean to investigate the catalyst structure, which could identify the oxygen de-fects on CeO_2 based materials. The visible Raman was carried out to investigate the CR, CP, and CC supports before and after immobilizing Au-Pd nanoparticles. As shown in Fig. 2, two bands were detected, the sharp peak between 462 and 465 cm^{-1} belonged to F_{2g} vibration mode, the small band peaked at 598 cm^{-1} could be attributed to oxygen de-fect-induced (D) mode [18]. The CR displayed a much broader F_{2g} peak compared to CP and CC, which further supports that CR has the smallest crystallite size analogously to the XRD results. The variation in peak linewidths of F_{2g} mode was previously reported as the size-dependent phenomenon detected in CeO_2, which could be interpreted as the phonon confinement and the inhomogeneous strain attributed to the particle size distribution [19]. According to the previous report [18], the amounts of oxygen defects on Ce-based catalysts have a positive correlation with the relative intensity ratio of I_D/I_{F2g}. For the tested CeO_2 supports, I_D/I_{F2g} value decreases in the following order; CR (0.1189) > CP (0.0309) > CC (0.0184), suggesting that the amounts of oxygen defects on CeO_2 is closely related to the morphologies of supports. After introducing Au-Pd nanoparticles on CeO_2, no bands attributed to Au or Pd nanoparticles were detected in these samples. It is interesting that the position of the peak assigned to F_{2g} vibration mode in Au-Pd/CeO_2 catalysts was shifted to lower wavenumber from bare CeO_2, which might be related to the formation of Ce-O-Au or Ce-O-Pd bonds. The I_D/I_{F2g} values of Au-Pd/CeO_2 catalysts were also calcu-lated and following the sequence; ACR (0.1329) > ACP (0.0804) > ACC (0.0649), which indicates that the amounts of oxygen defects were further enhanced compared with the pure CeO_2. Unlike Raman spectra, the shift of the peak position was not detected in XRD results, which could be related to the different range of measurement

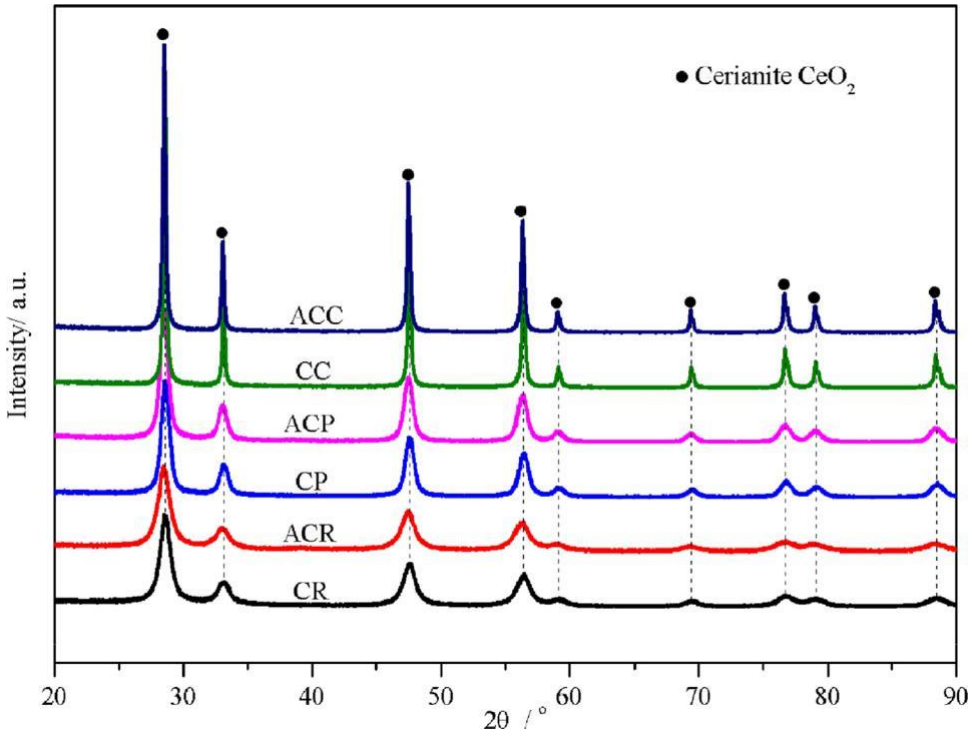

Fig. 1. XRD patterns of CR, ACR, CP, ACP, CC, and ACC samples.

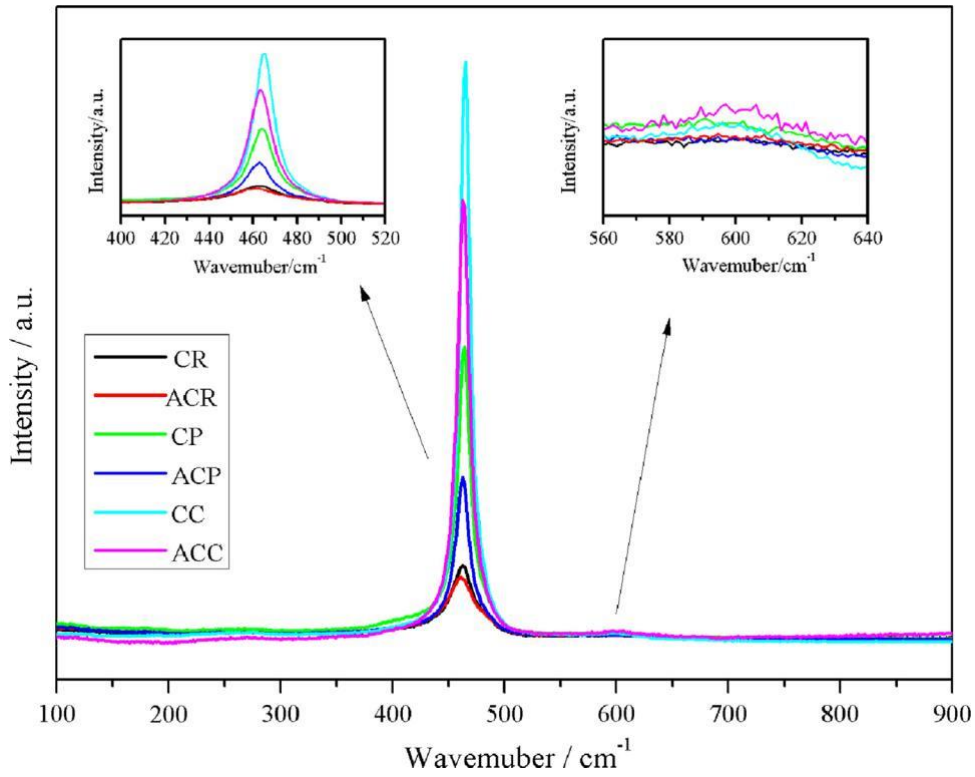

Fig. 2. Raman spectra of CR, ACR, CP, ACP, CC, and ACC samples.

between XRD and Raman scattering. The former is suitable for probing the long-range order materials and the latter is applied to examine the short-range order of crystallinity. By using Raman spectra, we con-firmed that the oxygen defects and the average CeO_2 particle size were intimately correlated to the different morphologies of CeO_2 supported catalysts.

TEM and HAADF-STEM were performed to analyze the crystal facets and morphology of the ACR, ACP, and ACC samples, together with the distribution of Au-Pd nanoparticle size. As shown in Fig. 3, each pre-pared Au-Pd/CeO_2 catalyst exhibits corresponding the rod, polyhedron, and cube shapes, respectively. Fig. 3a1 demonstrated TEM image of ACR with diameter of about 8 nm and the length about 40–100 nm. The regular interplanar spacing 0.27 nm of ACR was consistent with d value of {2 0 0} facet, indicating {1 0 0} facet of CeO_2 was selectively exposed on ACR surface based on the HRTEM image result in Fig. 3a2. As pre-viously reported, ceria nanorod usually grows along (1 0 0) direction with exposed {1 1 0} and {1 0 0} facets [20], which is consistent with our results. TEM and HRTEM images of ACP were exhibited in Fig. 3b. From the microscopy data we can see that the average size of ACP was about 13 nm, the spacing between lattice fringes was measured to be 0.31 nm and this value is in alignment with interplanar spacing of (1 1 1), suggesting that ACP is covered by {1 1 1} facets. In addition, microscopy results in Fig. 3c showed that the particle size of ACC was mainly distributed between 15 nm and 60 nm, two interplanar spacings of 0.31 and 0.27 nm were detected, indicating the surface of ACC was enclosed by {1 1 1} and {1 0 0} facets. Particle size distribution of AuPd nano particles on each support was characterized using HAADF-STEM. Based on measuring over 100 particles from the STEM results, it could be found that the bimetallic Au-Pd nanoparticles stay 3.05 nm in size on ACR sample. Meanwhile, ACP and ACC catalysts showed a similar Au-Pd particle size distribution compared to ACR, with the corresponding values of 3.23 nm and 2.92 nm. Therefore, it is conducted that the distribution of Au-Pd NPs on all the CeO_2 supports are less affected by the support morphology and the exposed crystal facet.

XPS is a surface sensitive technology which could provide quantitative and qualitative information of surface elements. In the present work, XPS was carried out to characterize the composition and chemical state of elements on the surface of Au-Pd/CeO_2 catalysts. Fig. 4a and b exhibited the XPS spectra of Au 4f and Pd 3d, respectively. As reported, the typical binding energies located at 87.7 and 84.0 eV could be attributed to the Au $4f_{5/2}$ and Au $4f_{7/2}$ signal of Au^0, respec-tively [21]. As shown in Fig. 4a, two peaks located at 87.3 and 83.6 eV were detected on the ACR sample, which shifted to lower binding en-ergy compared with the standard values. The similar negative shifts were also observed for ACP and ACC catalysts, which may be related to the electron transfer from CeO_2 to Au and electronic decoration of Au species by combining with Pd, suggesting the existence of strong in-teraction between Pd and Au [4]. The electron transfer from CeO_2 to Au would occur in Au-Pd/CeO_2 catalysts, because the work function of CeO_2 (4.69 eV) is lower than that of Au (5.31–5.47 eV) [22]. It is no-teworthy that gold is mostly present as Au^0 in these samples and no ionic Au species attributed to Au^{3+} (89.6 eV, 87.0 eV) and Au^+ (88.5 eV, 84.6 eV) were detected on the prepared Au-Pd/CeO_2 samples.

XPS spectra of Pd 3d on the ACR, ACP, and ACC were depicted in Fig. 4b. As reported, the bands of Pd 3d could be deconvoluted into sub-peaks and the binding energies for metallic Pd (Pd^0) and ionic Pd^{2+} species should be in the range of 334.8–336.2 eV and 336.2–338.7 eV, respectively [23]. It is clear that both metallic Pd and ionic Pd^{2+} were detected in the prepared ACP and ACC catalysts. However, only ionic Pd^{2+} could be detected in the ACR catalyst. The peaks at 337.7 and 342.9 eV are ascribed to $3d_{5/2}$and $3d_{3/2}$ orbits of ionic Pd^{2+}, whereas the binding energies at 335.7 and 335.2 eV belong to the $3d_{5/2}$ orbits of metallic Pd^0. The percentages of Pd^{2+} species present in Au-Pd/CeO_2 catalysts were obtained by calculation of the fitting areas Pd^{2+}/ (Pd^{2+}+Pd^0). Obviously, the concentrations of Pd^{2+} in Au-Pd/CeO_2 catalysts decreased as the following order: ACR (100%) > ACP (85.9%) > ACC (76.3%). It is acknowledged that the production of ionic Pd^{2+} was closely related to the catalyst surface oxygen species, which could supply oxygen to the Pd particles due to the high redox property.

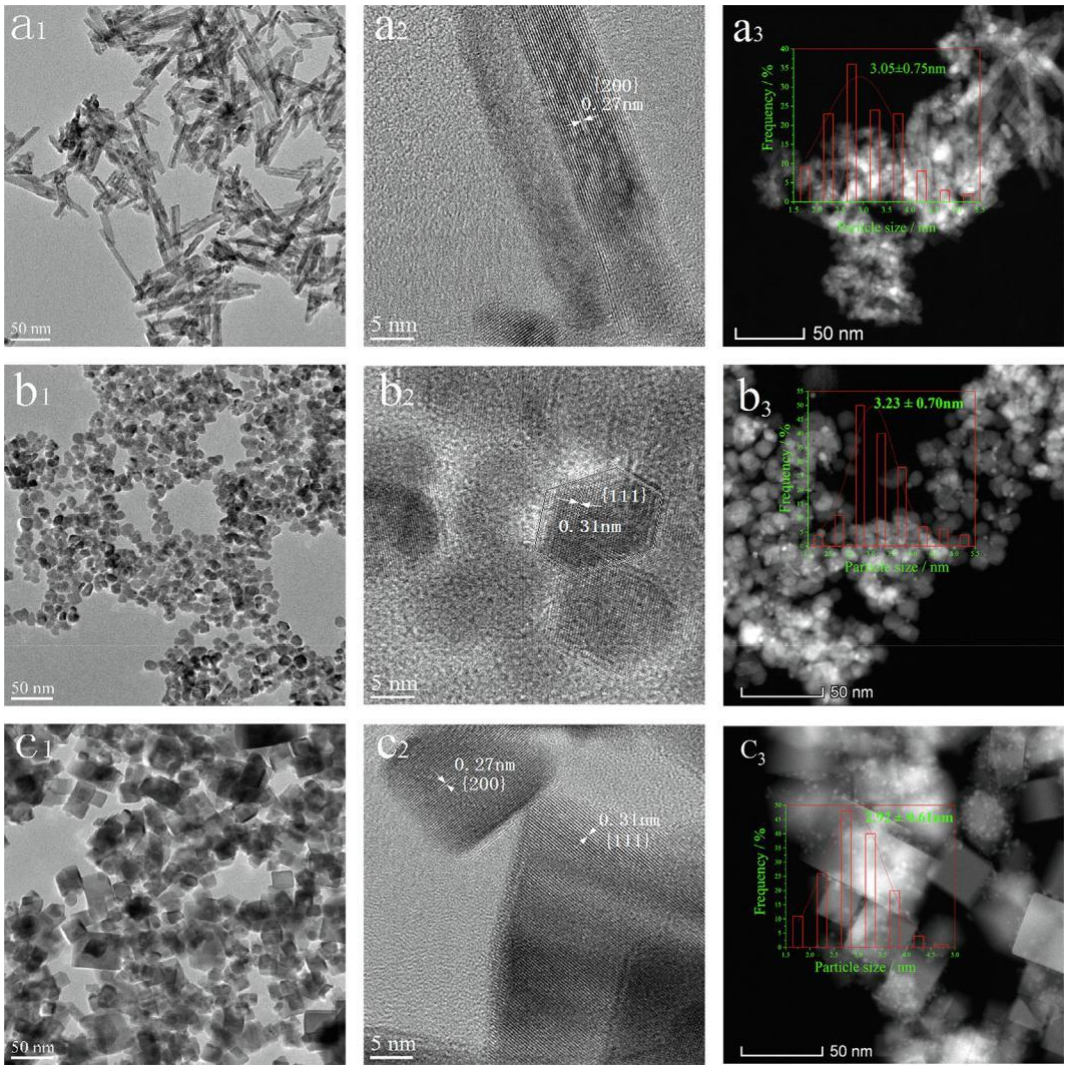

Fig. 3. TEM, HRTEM, HAADF STEM images and Au-Pd particle size distribution histograms of ACR (a_1, a_2, a_3), ACP (b_1, b_2, b_3), and ACC (c_1, c_2, c_3) catalysts.

Fig. 4c showed the Ce 3d XPS spectra in the ACR, ACP, and ACC catalysts, which could be fitted by eight sub-peaks based on the pre-vious reports. The four peaks between 880 eV and 899 eV corre-sponding to v, v′, v″, and v‴ components are attributed to $3d_{5/2}$ features and the rest of four peaks between 900 eV and 918 eV labeled as u‴, u″, u′, and u are attributed to $3d_{5/3}$, respectively. Meanwhile, u‴ compo-nent is a fingerprint of Ce^{4+} state which does not have $4f^0$ state. It was known that the components u′ and v′ are characteristics of Ce^{3+} and u, u″, u‴, v, v″, and v‴ are characteristics of Ce^{4+}. The equation of $Ce^{3+}/(Ce^{3+} + Ce^{4+})$ was applied to calculate the Ce^{3+} ratios on each cat-alyst based on the peak area and the corresponding results were also listed in Fig. 4c. The analysis results demonstrated that Ce^{4+} is the dominant oxidation state in all Au-Pd/CeO_2 catalysts and the Ce^{3+} ratio on ACR surface (14.8%) is higher than that on ACP (13.7%) and ACC (12.9%). It has been reported that two oxygen vacancies could be generated by one Ce^{3+}, so the higher proportion of Ce^{3+} implies a higher amount of oxygen vacancy on the catalyst surface [24]. Thus, the above analysis has further confirmed that more oxygen vacancies existed in ACR catalyst, which fit well with the Raman's results men-tioned before.

O1s XPS spectra for Au-Pd/CeO_2 catalysts were displayed in Fig. 4d. The sub-band at 529.4–529.7 eV should be attributed to the lattice oxygen (marked as Oβ), another sub-band detected at 531.5 eV-531.8 eV should be due to the surface adsorbed oxygen (labeled as Oα), respectively [25]. It is assumed that the surface adsorbed oxygen shows higher mobility than lattice oxygen, Oα not only can stabilize Au-Pd nanoparticles, but also facilitate the catalytic oxidation reaction. Thereafter, the content of Oα was estimated by using Oα/(Oα + Oβ), the calculation results demonstrated that the Oα on ACR (32.4%) is higher than that on the ACP (31.4%) and ACC (31.7%) , which is in align with the sequence of Ce^{3+} ratios observed on the catalyst surface.

The surface atomic composition derived from the XPS results was listed in Table 3. Compared with ICP-AES results, it could be found that the concentrations of Pd on the surface of ACR, ACP, and ACC catalysts were higher than that in the corresponding bulk. In contrast, the con-centration of Au detected on the catalyst surface was lower than the value in bulk. Based on the observed Pd and Au elements on the cata-lysts by using XPS, the molar ratios of Au/Pd were calculated and ranked by ACP > ACR > ACC. These values based on the XPS characterization were found lower than the nominal Au/Pd values, which suggests the enrichment of Pd species on CeO_2 surface, the si-milar phenomenon was also reported by David et al, which could be assigned to the variation in XPS analysis depths between Pd and Au [15].

4. Catalytic performance measurement

Au-Pd bimetal immobilized on different morphologies of CeO_2 were applied to investigate their reaction performance for solvent-free benzyl alcohol oxidation at 120 °C under 0.3 MPa O_2. The conversion of benzyl

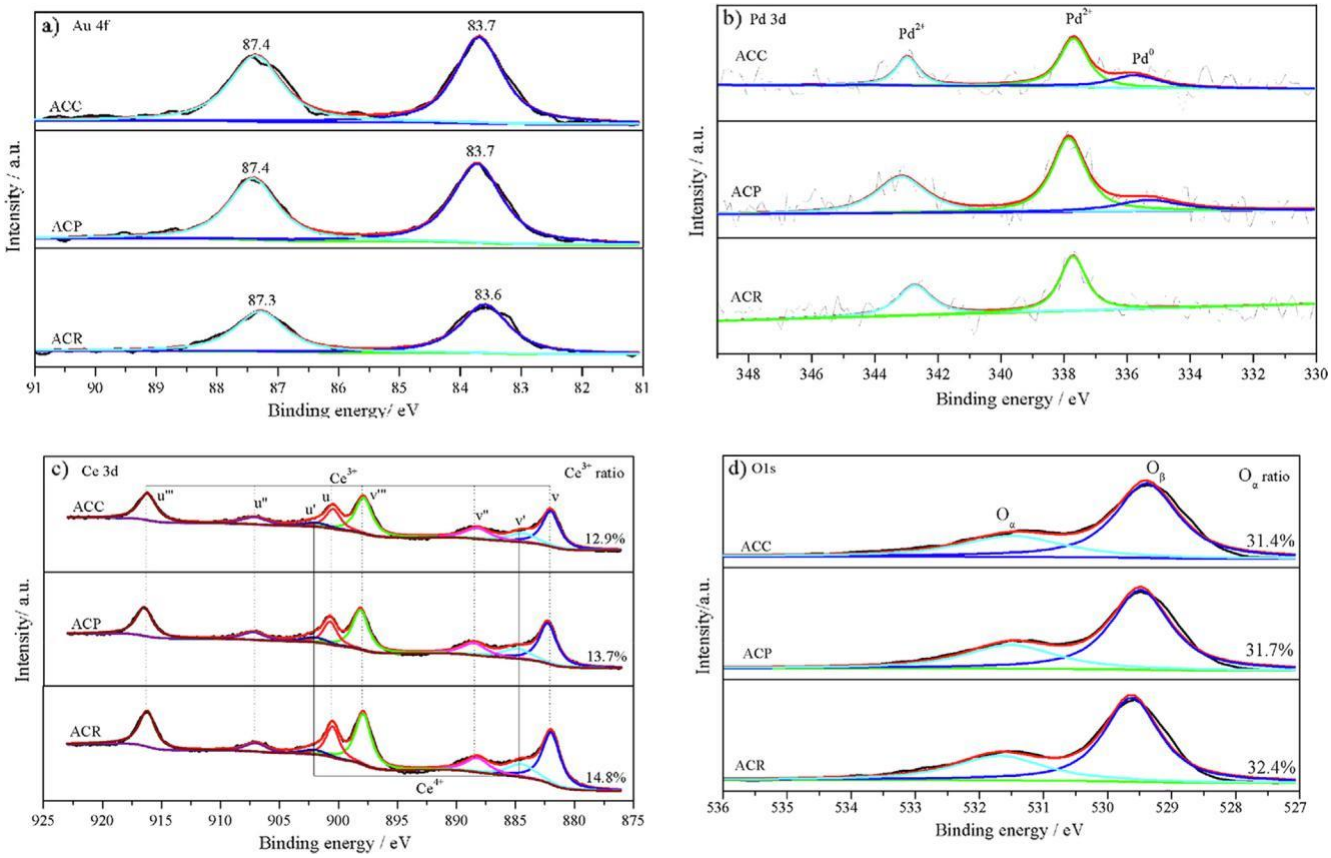

Fig. 4. XPS spectra of Au 4f (a), Pd 3d (b), Ce 3d (c) and O 1s (d) for ACR, ACP, and ACC catalysts.

Table 3
Surface element composition on the Au-Pd/CeO_2 catalysts.

Catalysts	Surface Content (Atomic %)				Au/Pd molar ratio
	Au 4f	Pd3d	O1s	Ce3d	
ACR	0.45	0.85	77.05	21.64	0.29
ACP	0.88	1.35	76.62	21.15	0.35
ACC	0.93	1.95	76.55	20.57	0.26

Note: The surface element concentration was determined by XPS.

alcohol and the selectivity to benzaldehyde on the ACR, ACP, and ACC catalysts were exhibited in Fig. 5. The benzyl alcohol conversion over CeO_2 samples and the selectivities towards other generated products, such as benzene, benzoic acid, toluene, and benzyl benzoate on the CeO_2 and Au-Pd/CeO_2 catalysts are also listed in Table 4. Based on the experimental results of the present work, it is found that the primary product was benzaldehyde, which is consistent to those published works from AuPd catalysis [26,27]. Meanwhile, it also could be ob-served that CeO_2 support alone exhibited limited catalytic activity. As showed in Fig. 5, ACR catalyst exhibited the highest benzyl alcohol conversion of 78.15% after reaction carried for 3 h. By contrast, only 55.14% and 48.84% benzyl alcohol conversion could be achieved on ACP and ACC catalysts under the identical reaction conditions. In ad-dition, it was noteworthy that the benzyl alcohol conversion over ACC catalyst maintained almost the same after reaction for 2 h, which might be caused by the poisoning of Pd as Pd surface is saturated by benzyl aldehyde during the reaction. As it is widely reported that Pd can be easily deactivated due to the desorption problem of aldehyde products on the catalyst surface [28–31]. We suggest that Pd poisoning affected the conversion of ACC containing the highest amount of Pd (Au/Pd molar ratio of 0.26) on the catalyst surface according to XPS measurements. Fig. 5 shows that ACC displayed the highest selectivity to benzaldehyde (> 92%) within 6 h reaction compared with ACR and ACP, which is well in agreement to the explained phenomenon. Therefore, different morphologies of CeO_2 supports lead to a different exposed amount of Pd on the catalyst surface, which interact with re-actant molecules, affecting its catalysis performance in catalytic oxi-dation benzyl alcohol.

To further clarify the dependence between the catalytic perfor-mance and the property of catalyst structure, it is essential to calculate the turnover frequency (TOF) values for each Au-Pd/CeO_2 catalyst with different morphology in the catalytic conversion of benzyl alcohol. Generally, the catalytic conversion should be controlled below 15% when calculating TOF values. Therefore, the catalytic performance of each catalyst was compared at a reaction time of 0.5 h with less amount of added catalyst into the reaction (14 mg). The TOF results were ex-hibited in Fig. 6. Obviously, the highest TOF value (31,757 h^{-1}) was obtained on the ACR catalyst (benzyl alcohol conversion: 13.86%). While the ACP and ACC catalysts exhibited relatively lower catalytic activity with TOF values of 27,226 h^{-1} (benzyl alcohol conversion: 14.83%) and 10,339 h^{-1} (benzyl alcohol conversion: 4.55%) under the corresponding experimental conditions.

Based on all the characterization results and the catalytic activities tests, it could be inferred that the performances of Au-Pd/CeO_2 cata-lysts in solvent-free benzyl alcohol oxidation are indeed closely related to their physico-chemical properties from the different morphologies of the supports.

5. Conclusion

In conclusion, Au-Pd NPs were immobilized on CeO_2 with diverse morphologies through deposition-precipitation method, benzyl alcohol was used as the probe molecule for investigating catalytic activities

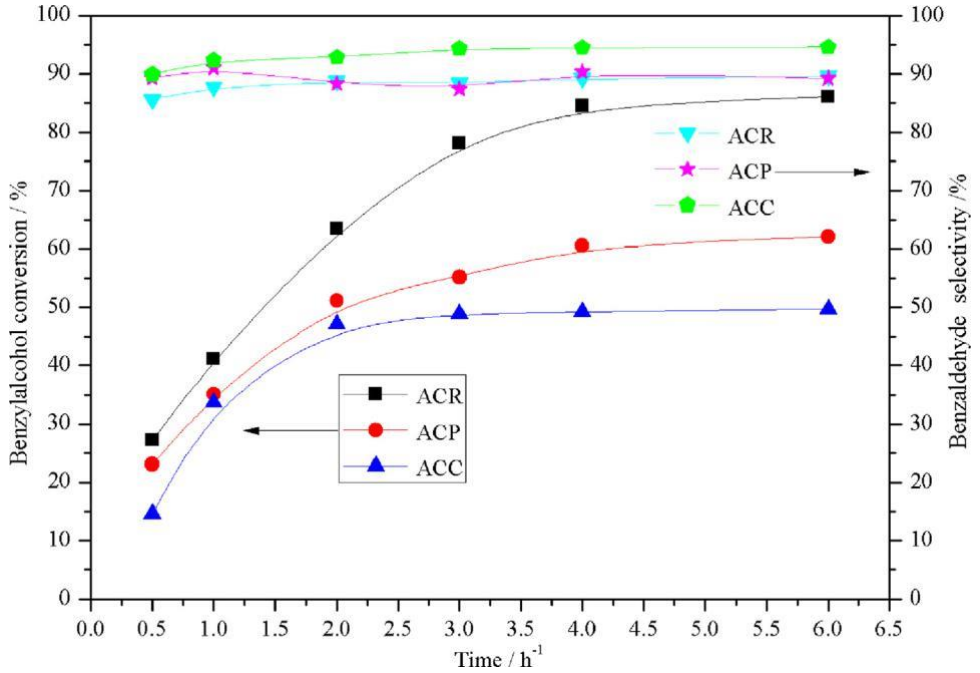

Fig. 5. Benzyl alcohol conversion and benzaldehyde selectivity as a function of time achieved on ACR, ACP, and ACC catalysts. Reaction conditions: catalyst mass 50 mg, temperature 120 °C, benzyl alcohol 15 mL, O_2 0.3 MP, stirring rate 1000 rpm.

Table 4
Oxidation of benzyl alcohol over CeO_2 and Au-Pd/CeO_2 catalysts at 120 °C under solvent-free.[a]

Sample	Conversion	Selectivity/%					
	%	Benzene	Toluene	Benzoic acid	Benzaldehyde	Benzyl benzoate	others
CR	0.91	1.08	8.20	–	83.41	7.31	–
ACR	78.15	0.23	5.21	0.31	88.43	5.54	0.28
CP	2.84	0.46	5.37	–	84.72	9.47	–
ACP	55.14	0.21	7.17	0.14	87.43	4.87	0.18
CC	1.13	1.22	5.64	–	88.63	4.51	–
ACC	48.84	0.65	3.05	0.18	94.33	1.57	0.22

[a] Reaction condition: Benzyl alcohol 15 mL, catalyst 50 mg, O_2 0.3 MPa, 120 °C 3 h.

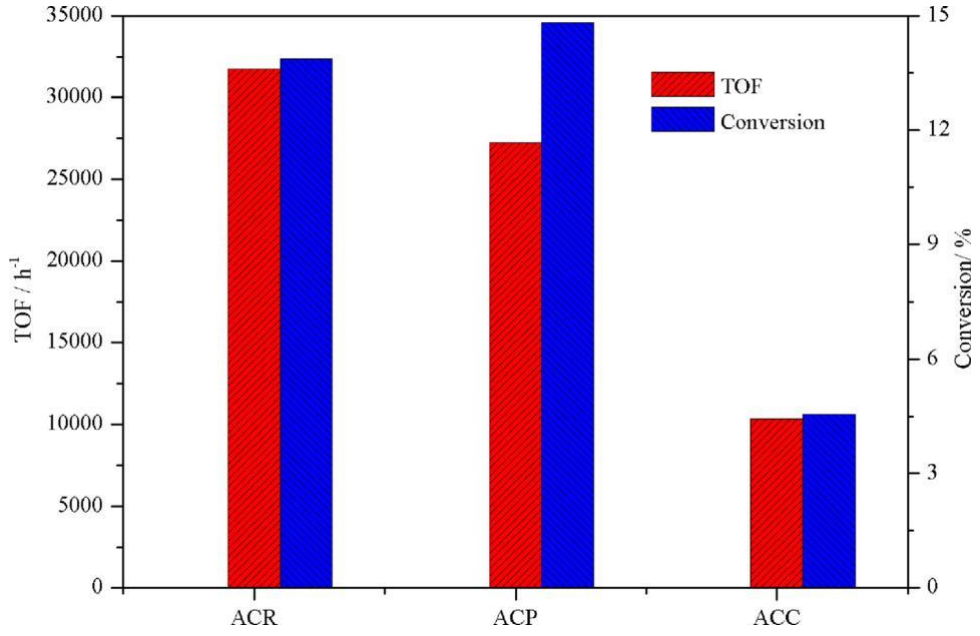

Fig.6. TOF values obtained on ACR, ACP, and ACC catalysts. Reaction conditions: catalyst mass 14 mg, reaction time 0.5 h, temperature 120 °C, benzyl alcohol 15 mL, O_2 0.3 MP, stirring rate 1000 rpm.

over each catalyst under solvent-free condition. The results of characterization and catalytic performance tests demonstrated that the catalytic activities for Au-Pd/CeO_2 in benzyl alcohol oxidation were largely dependent on CeO_2 morphologies, a rod-shape structure in the catalyst support (ACR) is more favoured compared with structures of polyhedrons (ACP) and cube (ACC). Series of characterization results of XRD, Raman, TEM, HAADF-STEM and XPS indicate that CeO_2 support of rod structure contains a higher concentration of oxygen defects, especially for O_α, a higher number of Ce^{3+} and Pd^{2+} on the catalyst surface, all these characters have played important roles in solvent-free benzyl alcohol oxidation.

Declaration of Competing Interest

The authors declared that there is no conflict of interest.

Acknowledgment

This work was supported by the National Natural Science Foundation of China (No. 21606162), the scholarship from China Scholarship Council (CSC) (No. 201706935068) and the Research Program of Science and Technology at Universities of Inner Mongolia Autonomous Region (NJZY19338).

References

[1] A. Villa, N. Dimitratos, C. Chan-Thaw, C. Hammond, L. Prati, G. Hutchings, Glycerol oxidation using gold-containing catalysts, Acc. Chem. Res. 48 (2015) 1403–1412.
[2] M. Flytzani-Stephanopoulos, Gold atoms stabilized on various supports catalyze the water-gas shift reaction, Acc. Chem. Res. 47 (2013) 783–792.
[3] E. Bus, R. Prins, J. Van Bokhoven, Origin of the cluster-size effect in the hydro-genation of cinnamaldehyde over supported Au catalysts, Catal. Commun. 8 (2007) 1397–1402.
[4] D. Enache, J. Edwards, P. Landon, B. Espriu, A. Carley, A. Herzing, M. Watanabe, C. Kiely, D. Knight, G. Hutchings, Solvent-free oxidation of primary alcohols to aldehydes using Au-Pd/TiO_2 catalysts, Science 311 (2006) 362–365.
[5] J. Edwards, E. Ntainjua, A. Carley, A. Herzing, C. Kiely, G. Hutchings, Direct synthesis of H_2O_2 from H_2 and O_2 over gold, palladium, and gold-palladium cata-lysts supported on acid-pretreated TiO_2, Angew. Chem. Int. Edit. 48 (2009) 8512–8515.
[6] N. Agarwal, S. Freakley, R. McVicker, S. Althahban, N. Dimitratos, Q. He, D. Morgan, R. Jenkins, D. Willock, S. Taylor, C. Kiely, G. Hutchings, Aqueous Au-Pd colloids catalyze selective CH_4 oxidation to CH_3OH with O_2 under mild conditions, Science 358 (2017) 223–227.
[7] L. Kesavan, R. Tiruvalam, M. Rahim, M. Saiman, D. Enache, R. Jenkins, N. Dimitratos, J. Lopez-Sanchez, S. Taylor, D. Knight, C. Kiely, G. Hutchings, Solvent-free oxidation of primary carbon-hydrogen bonds in toluene using Au-Pd alloy nanoparticles, Science 331 (2011) 195–199.
[8] Y. Chen, H. Lim, Q. Tang, Y. Gao, T. Sun, Q. Yan, Y. Yang, Solvent-free aerobic oxidation of benzyl alcohol over Pd monometallic and Au-Pd bimetallic catalysts supported on SBA-16 mesoporous molecular sieves, Appl. Catal. A. Gen. 380 (2010) 55–65.
[9] Y. Hong, X. Jing, J. Huang, D. Sun, A. Wubah, F. Yang, M. Du, Q. Li, Biosynthesized bimetallic Au-Pd nanoparticles supported on TiO2 for solvent-free oxidation of benzyl alcohol, ACS Sustain. Chem. Eng. 2 (2014) 1752–1759.
[10] A. Villa, D. Wang, N. Dimitratos, V. Trevisan, L. Prati, Pd on carbon nanotubes for liquid phase alcohol oxidation, Catal. Today 150 (2010) 8–15.
[11] R. Si, M. Flytzani-Stephanopoulos, Shape and crystal-plane effects of nanoscale ceria on the activity of Au-CeO_2 catalysts for the water-gas shift reaction, Angew. Chem. Int. Edit. 47 (2008) 2884–2887.
[12] D. Lee, Y. Chen, The mutual promotional effect of Au-Pd/CeO_2 bimetallic catalysts on destruction of toluene, J. Taiwan. Inst. Chem. Eng. 44 (2013) 40–44.
[13] H. Mai, L. Sun, Y. Zhang, R. Si, W. Feng, H. Zhang, H. Liu, C. Yan, Shape-selective synthesis and oxygen storage behavior of ceria nanopolyhedra, nanorods, and na-nocube, J. Phys. Chem. B 109 (2005) 24380–24385.
[14] H. Zhang, Y. Xie, Z. Sun, R. Tao, C. Huang, Y. Zhao, Z. Liu, In-situ loading ultrafine AuPd particles on ceria: Highly active catalyst for solvent-free selective oxidation of benzyl alcohol, Langmuir 27 (2010) 1152–1157.
[15] M. Khawaji, D. Chadwick, Au-Pd NPs immobilised on nanostructured ceria and ti-tania: impact of support morphology on the catalytic activity for selective oxida-tion, Catal. Sci. Technol. 8 (2018) 2529–2539.
[16] C. Olmos, L. Chinchilla, A. Villa, J. Delgado, H. Pan, A. Hungría, G. Blanco, J. Calvino, L. Prati, X. Chen, Influence of pretreatment atmospheres on the per-formance of bimetallic Au-Pd supported on ceria-zirconia mixed oxide catalysts for benzyl alcohol oxidation, Appl. Catal. A-Gene 525 (2016) 145–157.
[17] C. Olmos, L. Chinchilla, A. Villa, J. Delgado, A. Hungría, G. Blanco, L. Prati, J. Calvino, X. Chen, Size, nanostructure, and composition dependence of bimetallic Au-Pd supported on ceria-zirconia mixed oxide catalysts for selective oxidation of benzyl alcohol, J. Catal. 375 (2019) 44–55.
[18] B. Liu, C. Li, G. Zhang, X. Yao, S. Chuang, Z. Li, Oxygen vacancy promoting di-methyl carbonate synthesis from CO_2 and methanol over Zr-doped CeO_2 nanorods, ACS Catal. 8 (2018) 10446–10456.
[19] Z. Wu, M. Li, J. Howe, H. Meyer, S. Overbury, Probing defect sites on CeO_2 na-nocrystals with well-defined surface planes by Raman spectroscopy and O_2 ad-sorption, Langmuir 26 (2010) 16595–16606.
[20] C. Yang, X. Yu, S. Heißler, A. Nefedov, A. Nefedov, S. Colussi, J. Llorca, A. Trovarelli, Y. Wang, C. Wöll, Surface faceting and reconstruction of ceria na-noparticles, Angew. Chem. Int. Ed. 56 (2017) 375–379.
[21] T. Jaramillo, S. Baeck, B. Cuenya, E. McFarland, Catalytic activity of supported Au nanoparticles deposited from block copolymer micelles, J. Am. Chem. Soc. 125 (2003) 7148–7149.
[22] P. Huang, F. Wu, B. Zhu, X. Gao, H. Zhu, T. Yan, W. Huang, S. Wu, D. Song, CeO_2 nanorods and gold nanocrystals supported on CeO_2 nanorods as catalyst, J. Phys. Chem. B 109 (2005) 19169–19174.
[23] X. Meng, Z. Zhang, Bi_2MoO_6 co-modified by reduced graphene oxide and palladium (Pd^{2+} and Pd^0) with enhanced photocatalytic decomposition of phenol, Appl. Catal. B 209 (2017) 383–393.
[24] E. Bêche, P. Charvin, D. Perarnau, Ce 3d XPS investigation of cerium oxides and mixed cerium oxide ($Ce_xTi_yO_z$), Surf. Interface Anal. 40 (2008) 264–267.
[25] P. Dutta, S. Pal, M. Seehra, Y. Shi, E. Eyring, R. Ernst, Concentration of Ce^{3+} and oxygen vacancies in cerium oxide nanoparticles, Chem. Mater. 18 (2006) 5144–5146.
[26] N. Dimitratos, J. Lopez-Sanchez, D. Morgan, A. Carley, R. Tiruvalam, C. Kiely, D. Bethell, G. Hutchings, Solvent-free oxidation of benzyl alcohol using Au-Pd catalysts prepared by sol immobilization, Phys. Chem. Chem. Phys. 11 (2009) 5142–5153.
[27] M. Khawaji, D. Chadwick, Au-Pd bimetallic nanoparticles immobilised on titanate nanotubes: a highly active catalyst for selective oxidation, ChemCatChem 23 (2017) 4353–4363.
[28] J. Naughton, A. Lee, S. Thompson, C. Vinod, K. Wilson, Reactivity of crotonalde-hyde and propene over Au/Pd (111) surfaces, Phys. Chem. Chem. Phys. 12 (2010) 2670–2678.
[29] M. Bowker, L. Cookson, J. Bhantoo, A. Carley, E. Hayden, L. Gilbert, C. Morgan, J. Counsell, P. Yaseneva, The decarbonylation of acetaldehyde on Pd crystals and on supported catalysts, Appl. Catal. A. Gen. 391 (2011) 394–399.
[30] A. Lee, J. Naughton, Z. Liu, K. Wilson, High-pressure XPS of crotyl alcohol selective oxidation over metallic and oxidized Pd (111), ACS Catal. 2 (2012) 2235–2241.
[31] C. Parlett, L. Durndell, A. Machado, G. Cibin, D. Bruce, N. Hondow, K. Wilson, A. Lee, Alumina-grafted SBA-15 as a high performance support for Pd-catalysed cinnamyl alcohol selective oxidation, Catal. Today 229 (2014) 46–55.